Journal of
Applied Remote Sensing

Assimilation of clear sky Atmospheric Infrared Sounder radiances in short-term regional forecasts using community models

Agnes H. N. Lim
James A. Jung
Hung-Lung Allen Huang
Steven A. Ackerman
Jason A. Otkin

SPIE

Assimilation of clear sky Atmospheric Infrared Sounder radiances in short-term regional forecasts using community models

Agnes H. N. Lim,[a,b,*] **James A. Jung,**[a] **Hung-Lung Allen Huang,**[a] **Steven A. Ackerman,**[a] **and Jason A. Otkin**[a]

[a]University of Wisconsin-Madison, Cooperative Institute for Meteorological Satellite Studies, 1225 W. Dayton Street, Madison, Wisconsin 53706

[b]University of Wisconsin-Madison, Department of Atmospheric and Oceanic Sciences, 1225 W. Dayton Street, Madison, Wisconsin 53706

Abstract. Regional assimilation experiments of clear-sky Atmospheric Infrared Sounder (AIRS) radiances were performed using the gridpoint statistical interpolation three-dimensional variational assimilation system coupled to the weather research and forecasting model. The data assimilation system and forecast model used in this study are separate community models; it cannot be assumed that the coupled systems work optimally. Tuning was performed on the data assimilation system and forecast model. Components tuned included the background error covariance matrix, the satellite radiance bias correction, the quality control procedures for AIRS radiances, the forecast model resolution, and the infrared channel selection. Assimilation metrics and diagnostics from the assimilation system were used to identify problems when combining separate systems. Forecasts initiated from analyses after assimilation were verified with model analyses, rawinsondes, nonassimilated satellite radiances, and 24 h–accumulated precipitation. Assimilation of clear sky AIRS radiances showed the largest improvement in temperature and radiance brightness temperature bias when compared with rawinsondes and satellite observations, respectively. Precipitation skill scores displayed minor changes with AIRS radiance assimilation. The 00 and 12 coordinated universal time (UTC) forecasts were typically of better quality than the 06 and 18 UTC forecasts, possibly due to the amount of AIRS data available for each assimilation cycle. © *2014 Society of Photo-Optical Instrumentation Engineers (SPIE)* [DOI: 10.1117/1.JRS.8.083655]

Keywords: Atmospheric Infrared Sounder; radiance assimilation; gridpoint statistical interpolation; weather research and forecasting.

Paper 13457 received Nov. 17, 2013; revised manuscript received Feb. 20, 2014; accepted for publication Mar. 10, 2014; published online Apr. 2, 2014.

1 Introduction

Atmospheric Infrared Sounder (AIRS)[1,2] measures the Earth's upwelling radiances between 3.7 and 15.4 μm. The large number of channels (2378 channels) and relatively high spectral resolution enable the atmosphere to be sensed at a higher vertical resolution. AIRS has the capability to better resolve the large vertical variability in the atmosphere in terms of temperature and humidity than the broadband infrared (IR) sounders, which have fewer channels. Information content analyses by Refs. 3 and 4 revealed that the AIRS spectrum contained about 14 pieces of independent information in the vertical temperature profile, and this translates to ~1-km vertical resolution in the troposphere.[5,6] AIRS has a spatial resolution of 13.5 km.

Numerical weather prediction (NWP) centers around the world began assimilating AIRS radiances operationally into global models as early as 2003 (Ref. 7), and others followed soon after.[8–12] These centers reported improvement in global forecast skill with the assimilation

*Address all correspondence to: Agnes H. N. Lim, E-mail: alim@ssec.wisc.edu

of clear sky AIRS radiances. Regional satellite data assimilation poses even greater challenges than global data assimilation due to spatial and temporal limitations. The number of observations becomes highly variable at each assimilation cycle due to a smaller domain and typically shorter time windows between assimilation cycles. Uncertainty in land surface emissivity has limited the use of observations over land. In the regional case, the uneven distribution of land and sea coverage further varies the number of observations that can be assimilated. The current method requires a large-observation sample size, as coefficient predictors used to describe the biases are regressed against observations.[13] Limited data volume has a large impact on the bias correction method currently employed by most data assimilation systems, reducing the ability of the assimilation system to correct for biases.

Results from assimilating AIRS radiances in regional models have been mixed. Reference 14 saw positive impact on the analysis and subsequent short-term (0 to 48 h) forecasts with the assimilation of clear sky AIRS radiances. Using a similar hyperspectral IR instrument, Ref. 15 reported that the assimilation of Infrared Atmospheric Sounding Interferometer (IASI) radiances in the North Atlantic and European model had a neutral impact.

The data assimilation system and the regional forecast model used in this study were separate entities; therefore, it could not be assumed that the two systems work optimally together. The first step was to evaluate the performance of the combined assimilation system and forecast model. This evaluation should be done for all combined model and assimilation systems but was even more critical when they are not obtained directly from an operational NWP center. By looking at various assimilation metrics and the diagnostics generated when running the assimilation system, one could identify most of the problems when combining the separate systems. Tuning the two systems was an iterative process since tuning one component affects others. In this study, tuning was performed on the assimilation system and the forecast model. Components being tuned in the assimilation system included the quality control (QC) procedures, the background error covariance (**B**) matrix and the radiance bias corrections. The model tuning parameters included the vertical resolution of the forecast model and the IR radiance channel selection.

The article is structured as follows: Sec. 2 briefly outlines the data assimilation system and the NWP model used in this study as well as the experimental design. Section 3 discusses the various components of the data assimilation system being tuned. In Sec. 4, results obtained from the analysis of the performance of the assimilation system and forecast verification are presented. The results are summarized in Sec. 5.

2 Assimilation System, Forecast Model, and Experimental Design

2.1 *Weather Research and Forecasting Model*

The weather research and forecasting (WRF) model is a mesoscale NWP system developed by the National Center for Atmospheric Research (NCAR). It solves the compressible nonhydrostatic Euler equations cast in flux form on a mass-based terrain following vertical coordinate system.[16] The WRF model is suitable for a broad spectrum of applications across scales ranging from meters (large eddy simulations) to thousands of kilometers (global simulations). Applications include real-time NWP, data assimilation development and studies, parameterized-physics research, regional climate simulations, air quality modeling, atmosphere-ocean coupling, and idealized simulations. The model version used in this study was 3.2.1 and was released in August 2010.

Regional models require initial conditions to initiate the model and lateral boundary conditions (LBCs) to be provided at various time steps as the model integrates forward in time. Differences in resolution, physical process parameterizations, absence of feedback between synoptic and mesoscale processes, formulation of LBC, and the accuracies of models that provide the LBC introduce errors into regional models.[17] These errors could degrade the forecast skill of regional models.

The model domain had 624 by 357 horizontal gridpoints with a resolution of 13 km as shown in Fig. 1. The vertical resolution consisted of 75 sigma levels extending from surface to 2.5 hPa.

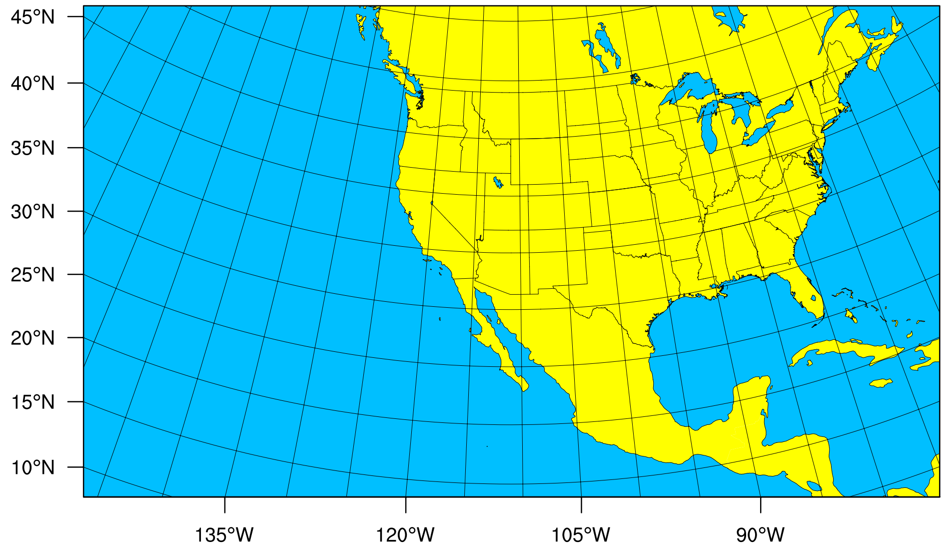

Fig. 1 The model domain extends from 7°N to 57°N and 53°W to 170°W. It had 624 by 357 gridpoints with a spatial resolution of 13 km. There were 75 sigma levels distributed between surface and 2.5 hPa.

The atmosphere used to initialize the regional model was the postprocessed pressure-grib (general regularly-distributed information in binary) files provided by the National Center for Environmental Prediction (NCEP) global forecasting system (GFS) at a frequency of 3 h. The grib files had a horizontal resolution of 1.0 deg latitude/longitude with 48 vertical levels and a model top of 1 hPa.

2.2 *Gridpoint Statistical Interpolation*

The data assimilation system was the gridpoint statistical interpolation (GSI) developed by NCEP and is described by Refs. 18 and 19. This was version 3.0 of the community code[20] that was released in April 2011. The GSI is a three-dimensional incremental variational system and is capable of assimilating a wide range of observations; spanning from conventional data such as rawinsondes, aircraft, ships, and buoys to satellite radiances. The GSI can be run for both global and regional scale applications. The analysis variables used in the GSI are streamfunction (ψ), unbalanced part of the velocity potential (χ), the unbalanced part of virtual temperature (T), the unbalanced surface pressure (P), and the pseudo relative humidity (RH) or normalized RH.[18,21]

The GSI was run in regional mode with an isotropic and spatially inhomogeneous background error covariance (**B**) matrix. Normalized RH was used as its moisture analysis variable. The normalized RH allows for a multivariate coupling of the moisture, temperature, and pressure increments.[19] The results from the GSI provided the initial conditions for the WRF model.

In satellite radiance assimilation, it was necessary to compute the NWP model equivalent of the radiance observations. Version 2.0.2 of the community radiative transfer model (CRTM)[22–25] was used as the forward operator to transform the grid point analysis to observation space and vice versa. The CRTM simulates both microwave and IR radiances observed by instruments onboard satellites for a given state of the atmosphere and the Earth's surface. The CRTM includes components that compute the gaseous absorption of radiation, absorption, and scattering of hydrometers and aerosols. It also computes emission and reflection of radiation by the ocean, land, snow, and ice surfaces. Besides the forward model, the corresponding tangent linear, adjoint, and K (Jacobian) matrix models were also developed to calculate the gradient and sensitivity of radiance with respect to the state variables. The transmittance models used in the CRTM are regression-based models, and in this study we have used the optical depth in pressure space model as explained in Ref. 25.

Table 1 Types of data used in assimilation.

Conventional	
Observation	Platform
	Sonde
Upper-air	Aircraft
	Profiler
Land surface	Surface sondes
	Metar
Marine surface	Ships
	Buoys
Radar	NEXRAD VAD
Satellite	
Observation	Platform
Satellite winds	GOES
Microwave radiances	AMSU-A
	MHS
Infrared radiances	HIRS-4
	Atmospheric Infrared Sounder

2.3 *Experimental Setup*

In this study, both conventional and satellite data were assimilated in the baseline experiment or control (CNTRL). Satellite data included in the CNTRL were data from the Advanced Microwave Sounding Unit (AMSU-A), the Microwave Humidity Sounder (MHS), and High resolution Infrared Radiation Sounder (HIRS-4). The complete list of data assimilated is given in Table 1. Radiance data were the dominant dataset. As observations are assumed to be independent, and observational errors are assumed to be uncorrelated; thinning was applied to all of the satellite radiances. The thinning mesh of 60 km used by the NCEP operational regional system was adopted except for HIRS-4, which had a thinning mesh of 120 km. The IR sensor channels were tested using Ref. 14, and channels with significant contributions above the model top were not used. Channels assimilated in the CNTRL are listed in Table 2.

Table 2 List of AMSU-A, MHS, and HIRS-4 channels used in the assimilation experiments.

Satellite	Sensor	Channels assimilated
NOAA-15	AMSU-A	1-10, 11-13 and 15
NOAA-18	AMSU-A	1-8, 10-13 and 15
	MHS	1-5
METOP-A	AMSU-A	1-6, 8-13 and 15
	MHS	1-5
	HIRS-4	4-8 and 10-15

The experiment (EXP) contained all of the data used in the CNTRL plus the clear sky AIRS radiances. The AIRS near real time dataset selected by Ref. 26 contained 281 channels of which only 83 were assimilated (Table 3). Channels removed by our QC included noisy or "popped" channels, shortwave channels, and ozone and other trace gas absorption features. Similar to the CNTRL, AIRS channels determined to have a significant contribution above the model top of 2.5 hPa using Ref. 14 were not used. These channels were assimilated over both land and sea. The AIRS data were also thinned to 60 km. The observational errors used for the AIRS channels assimilated were obtained from the NCEP's Global Data Assimilation System and are provided in Table 3. The noise equivalent differential temperatures (NEDT) provided in Table 3 were obtained from http://disc.sci.gsfc.nasa.gov/AIRS/documentation/v5_docs/AIRS_V5_Release_User_Docs/channel_properties_files/L2.chan_prop.2005.03.01.v9.5.1.txt.

Five assimilation cycles were performed at 3-h intervals, prior to running the forecast model out to 36 h (Fig. 2). A cold start was initiated at T-12 h. The initial background state was interpolated from the global analysis valid at this time, to the regional scale. Observations within a time window of ± 1.5 h of the center time were assimilated. This T-12 analysis was then used to initiate a 3-h short-term WRF forecast, which was used as a first guess for the next (or T-9) assimilation cycle. The 3-h forecast and data assimilation cycle were repeated through T-0. A 36-h forecast was then executed.

By cycling the assimilation, the initial conditions were updated by available observations every 3 h. The 3-h forecast contributed information from earlier observations into the current analysis. Assimilation experiments were started at each synoptic time 00, 06, 12, and 18 UTC. This study was conducted for a period of 16 days between May 17 and June 1, 2008.

3 Assimilation System Performance and Tuning

Prior to carrying out the experiments, tuning was required on the assimilation system. The components tuned included the QC procedures for IR radances, the (**B**) matrix, and the bias correction coefficients for satellite radiances. The performance of the assimilation system was evaluated by looking at various diagnostics generated within the assimilation system.

3.1 *QC of AIRS Radiances*

IR satellite observations are very sensitive to the presence of clouds. In this study, only clear sky AIRS observations were assimilated, as this version of GSI used has no explicit mechanism for assimilating cloudy radiances. Thus, cloud-affected observations should be filtered out before the assimilation. When AIRS field-of-view (FOVs) were read in by the GSI, threshold and difference tests were used to test for clouds. Over land and water, three different threshold tests using combinations of shortwave (4 μm) and longwave (11 μm) thermal channels were applied to identify clouds during the night. For water surfaces, observations were further checked against an estimated sea surface temperature derived from AIRS measurements. For cloud checks over snow and ice, tests were based on differences in absorption coefficients between ice and water.[27] The AIRS spectrum associated with the FOV that was the closest to the center of the thinning box and had passed the cloud tests was selected. This selected AIRS spectrum was further checked for cloud contamination on a channel basis. The observed bias-corrected channel brightness temperature was compared with that derived from the model, and a channel was determined to be clear if the contribution from the transmittance at and below a cloud layer was <2%.

The cloud detection routines within GSI are rather relaxed. Additional cloud check had been applied to the original AIRS data to select clear observations. An AIRS cloudmask was generated following Ref. 28, which used the cloud products from the moderate-resolution imaging spectrometer (MODIS) that is also on the AQUA spacecraft. Cloud properties of AIRS were characterized using a collocated 1-km MODIS cloudmask.[29] The MODIS cloudmask was derived based on a combination of the confidence of 40 different spectral tests used to identify clouds. For each AIRS footprint, a cloud fraction between 0 and 1 was calculated by determining the percentage of MODIS pixels that were flagged as cloudy. An AIRS footprint was determined to be clear if the percentage of potentially cloudy MODIS pixels collocated within the AIRS FOV was <1%. This new AIRS dataset was then written to a binary universal form for the representation of meteorological data (BUFR) file, which was read by the GSI.

Table 3 List of 83 AIRS channels used in the assimilation experiments with the corresponding wavenumber (ν), the peak weighting function (PWF), the observational error (R) used, as well as the noise equivalent difference temperature (NEDT) for a scene temperature of 250 K.

Chn	ν (cm^{-1})	PWF (hPa)	R	NEDT
156	694.397	185	0.900	0.3110
162	696.050	218	0.850	0.3244
168	697.710	241	0.950	0.3133
174	699.379	254	1.000	0.2931
175	699.658	229	0.850	0.2860
180	701.056	266	1.000	0.2760
186	702.741	280	0.900	0.2887
190	703.869	307	1.000	0.2769
192	704.434	321	0.900	0.2817
198	706.136	367	0.900	0.2507
201	706.990	351	0.900	0.2552
204	707.846	383	0.900	0.2605
207	708.704	367	0.900	0.2878
210	709.564	399	1.400	0.2948
215	711.003	451	0.850	0.2547
221	712.737	545	0.900	0.2559
226	714.189	672	0.900	0.2343
227	714.480	586	0.900	0.2366
232	715.939	718	0.900	0.2564
252	721.837	672	0.900	0.2513
253	722.134	650	0.850	0.2390
256	723.028	840	0.850	0.2401
257	723.326	840	0.900	0.2391
261	724.523	866	0.900	0.2412
262	724.822	840	0.900	0.2434
267	726.325	840	0.900	0.2605
272	727.833	840	0.900	0.2748
295	734.150	840	0.900	0.3568
299	735.381	815	0.900	0.2431
305	737.236	815	0.900	0.3906
310	738.788	790	0.900	0.3742
321	742.227	525	1.150	0.5686
325	743.485	840	0.900	0.3274
333	746.014	972	0.900	0.2499

Table 3 (*Continued*).

Chn	ν (cm^{-1})	PWF (hPa)	R	NEDT
338	747.603	918	0.900	0.3562
355	753.057	892	0.900	0.3191
362	755.326	918	0.900	0.2405
375	759.574	1028	0.900	0.3236
475	801.102	1057	0.950	0.2769
484	804.389	1057	0.950	0.3910
497	809.183	1085	0.950	0.3361
528	820.837	1085	0.950	0.4184
587	843.917	1085	0.900	0.3016
672	871.284	918	0.925	0.2051
787	917.303	1085	0.900	0.1102
791	918.744	1085	0.900	0.1385
870	948.182	972	0.900	0.2053
914	965.429	1085	0.850	0.1226
950	979.128	1085	0.800	0.0946
1301	1236.540	1000	0.800	0.0766
1304	1238.110	1085	0.700	0.0768
1329	1251.360	945	0.850	0.0855
1371	1285.480	866	1.100	0.0948
1382	1291.710	866	0.850	0.1030
1415	1310.770	766	2.500	0.1167
1424	1316.060	628	2.500	0.1216
1449	1330.980	815	2.500	0.1493
1455	1334.810	742	2.500	0.1569
1477	1345.310	742	2.500	0.1439
1500	1357.230	672	2.500	0.1245
1519	1367.250	628	2.500	0.1180
1565	1392.150	545	2.500	0.1020
1574	1397.135	433	2.500	0.0781
1627	1427.229	525	2.500	0.0825
1669	1468.830	433	2.500	0.0929
1694	1484.370	433	2.500	0.0910
1766	1544.480	293	2.500	0.1246
1800	1567.890	336	2.500	0.1499
1826	1586.260	487	2.500	0.1918

Table 3 (*Continued*).

Chn	ν (cm^{-1})	PWF (hPa)	R	NEDT
1865	2181.490	1085	0.600	0.1200
1866	2182.400	1085	0.650	0.1193
1868	2184.210	1000	0.600	0.1191
1869	2185.120	918	0.550	0.1217
1872	2187.850	972	0.500	0.0888
1873	2188.760	1057	0.525	0.0873
1876	2191.500	1085	0.550	0.0878
1881	2196.070	742	0.500	0.0898
1882	2196.990	718	0.500	0.0921
1911	2223.940	790	0.555	0.1002
1917	2229.590	433	0.575	0.1043
1918	2230.540	383	0.550	0.1059
1924	2236.230	336	0.650	0.1126
1928	2240.030	307	0.700	0.1125

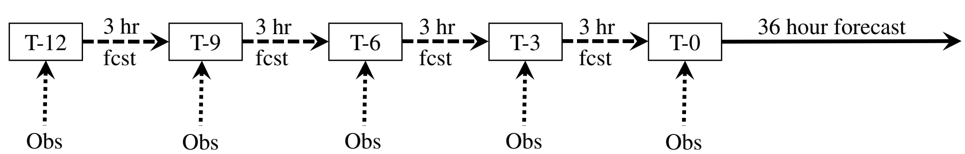

Fig. 2 Assimilation cycles valid for both control (CNTRL) and experiment (EXP). *T-N* (where *N* is the number of hours prior to initiating the forecast) is the analysis time. The initial condition at T-12 was interpolated from the NCEP global analysis which has a horizontal resolution of 1 deg latitude/longitude with 48 vertical levels and a model top of 1 hPa. Dashed arrows referred to 3-h weather research and forecasting short-term forecast for the next assimilation cycle. Dotted arrows indicate that observations (Obs) within a time window of ± 1.5 h were assimilated at this time. Solid arrow was a 36-h forecast.

3.2 *B* Matrix

The roles played by the **B** matrix are to spread out information from observations, control the percentage of the innovation [observation (O)-first guess (F)] that contributes to the analysis, and maintain dynamically consistent increments between model variables.[30] A poorly specified **B** matrix results in analysis increments [analysis (A)–first guess (F)] that are too large or too small. When this happens, the use of the observations and the first guess are not optimal.

Two sets of precomputed background error statistics were provided with the GSI. Both were estimated using the "NMC" method.[31] The **B** matrix derived using forecasts from the GFS will be known as global in this context and the other, which used forecasts from the NCEP operational regional system, will be called regional. The global **B** matrix had a global coverage (i.e., latitude coverage from 90°N to 90°S) whereas the regional **B** could only be used for domain coverage between 90°N and 2.5°S. More details on these two matrices can be found in Ref. 20. These matrices act as starting point of **B** matrix for a 3-h forecast. Adjustments were needed, as the **B** matrix is sensitive to both domain resolution and synoptic situation. Using a 12-h forecast difference to estimate the forecast error for a 3-h forecast will be too large.

Pseudo single observation tests (PSOT) were run not only to verify that the assimilation system was set up correctly but also to understand its impact. This provided some guidance to the tuning of the **B** matrix. When performing PSOT, a single "bogus" temperature observation was assimilated at the center of the domain. As the **B** matrix is multivariate, a perturbation in temperature causes a change in wind field through balanced properties that shows up as correlations in the **B** matrix. Figure 3 shows the adjustment in temperature, u-component, and v-component of wind due to a 1-K perturbation in temperature of the pseudo observation projected on the xy plane when applied to both the global and regional **B** matrices. The perturbation was placed at approximately the center of the domain (34°N, −111°E) and at 250 hPa (σ level 37). Both the global and regional **B** matrices had similar structures. The response due to the perturbation was isotropic. The analysis increments revealed that the horizontal scale of influence for various model variables was larger for the global **B** compared with the regional **B**. In addition, the magnitude of the adjustment was also larger for the global **B** matrix.

The vertical scale of influence for temperature looked similar for both the global and regional **B** except [Fig. 4(a)] where the vertical distribution of temperature increments showed a secondary maximum near the model top for the regional **B** matrix. For u-component of wind, the vertical scale of influence was larger for the global matrix. Similarly for u-component of wind, the secondary dipole was also located at a higher model level [Fig. 4(b)]. This implied a larger correction will be made at higher model levels from observations located lower in the atmosphere.

Analysis increments obtained from assimilating conventional data using the two different **B** matrices were compared to decide which matrix should be adopted for this study. Figure 5 shows

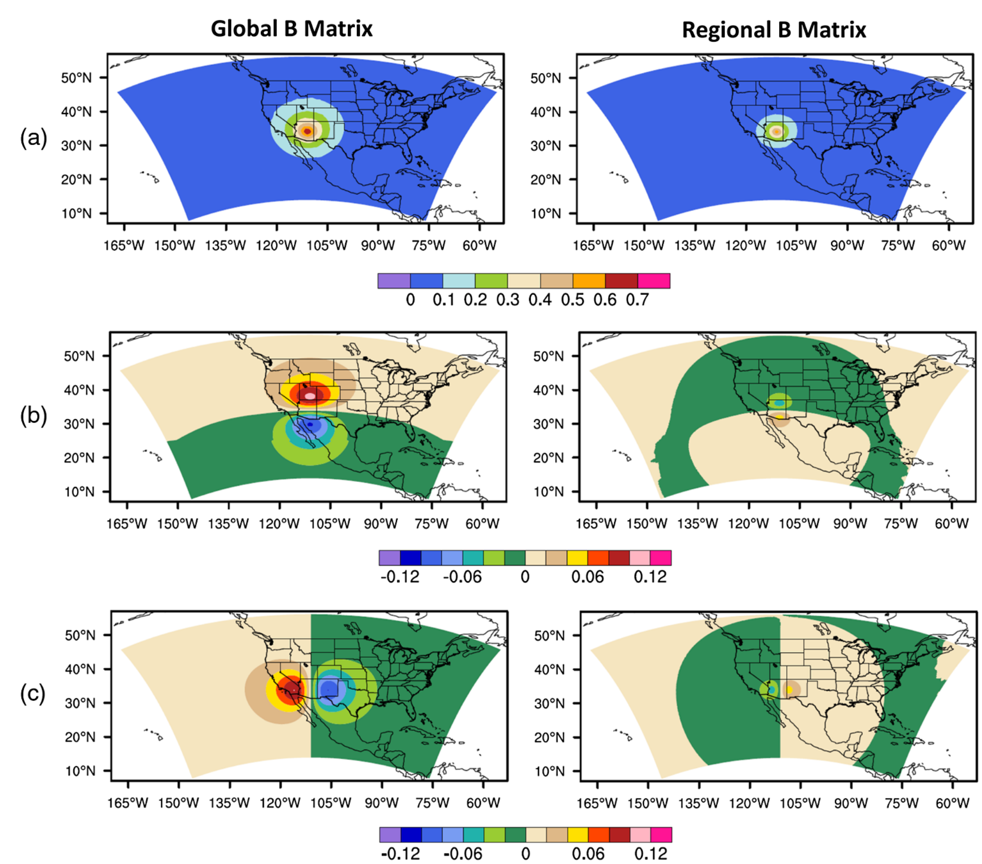

Fig. 3 Analysis increment on the xy plane at σ level 37 for a single temperature observation placed at 34°N, −111°E and 250 hPa for the global and regional **B** matrices. The difference between temperature observation and background is 1 K. Observational error is set to 1 K. (a) Temperature (K), (b) u-component of wind (ms^{-1}), and (c) v-component of wind (ms^{-1}).

the temperature analysis increment from using the two different **B** matrices. Figure 5(a) is the regional **B** matrix and Fig. 5(b) is the global **B** matrix. Only the highest 20 σ levels were plotted in Fig. 5, which corresponded to the region between ∼2 and 100 hPa. The regional **B** matrix resulted in a much larger temperature increment compared with that of the global **B** matrix on the topmost 6 layers of the atmosphere. As there are very little conventional data in the region between 2 and 15 hPa, the increment comes mostly from the vertical spreading of information from the lower atmosphere by the **B** matrix. This was consistent with the second maximum seen in PSOT. The increment in the stratosphere should be minimal for the reason that the stratosphere is a reasonably stable region of the atmosphere. On this basis, the **B** matrix based on the GFS model covering the global grid was chosen for this study.

After selecting the **B** matrix, assimilation runs were then conducted with the addition of satellite radiances. Upon the addition of satellite radiances, the magnitude of analysis increment for temperature was again greater than expected over large regions in the stratosphere. The magnitude of temperature analysis increment was decreased by reducing the background error amplitude weights for streamfunction and unbalanced virtual temperature variance in the **B** matrix. The choice for these two variables was guided by the design of the **B** matrix,[18] as the streamfunction defines a larger percentage of the temperature, velocity potential, and surface pressure increment. By decreasing variances of the **B** matrix, more confidence was placed on the short-term forecast. Tests were run for different combinations of amplitude weights for streamfunction, virtual temperature, and velocity potential. The combination that gave the most reasonable

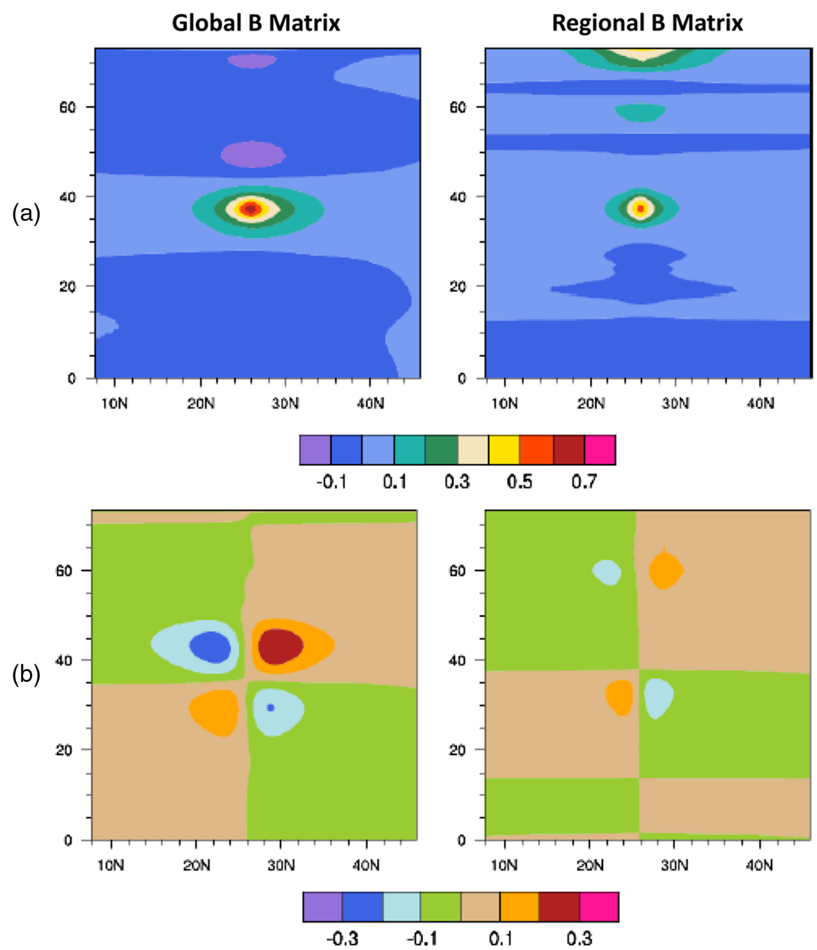

Fig. 4 Analysis increment on the *yz* plane at σ level 37 for a single temperature observation placed at 34°N, −111°E and 250 hPa for the global and regional **B** matrices. The vertical axis is the model levels with 0 referring to the surface.The difference between temperature observation and background is 1 K. Observational error is set to 1 K. (a) Temperature (K), (b) u-component of wind (ms^{-1}), and (c) v-component of wind (ms^{-1}).

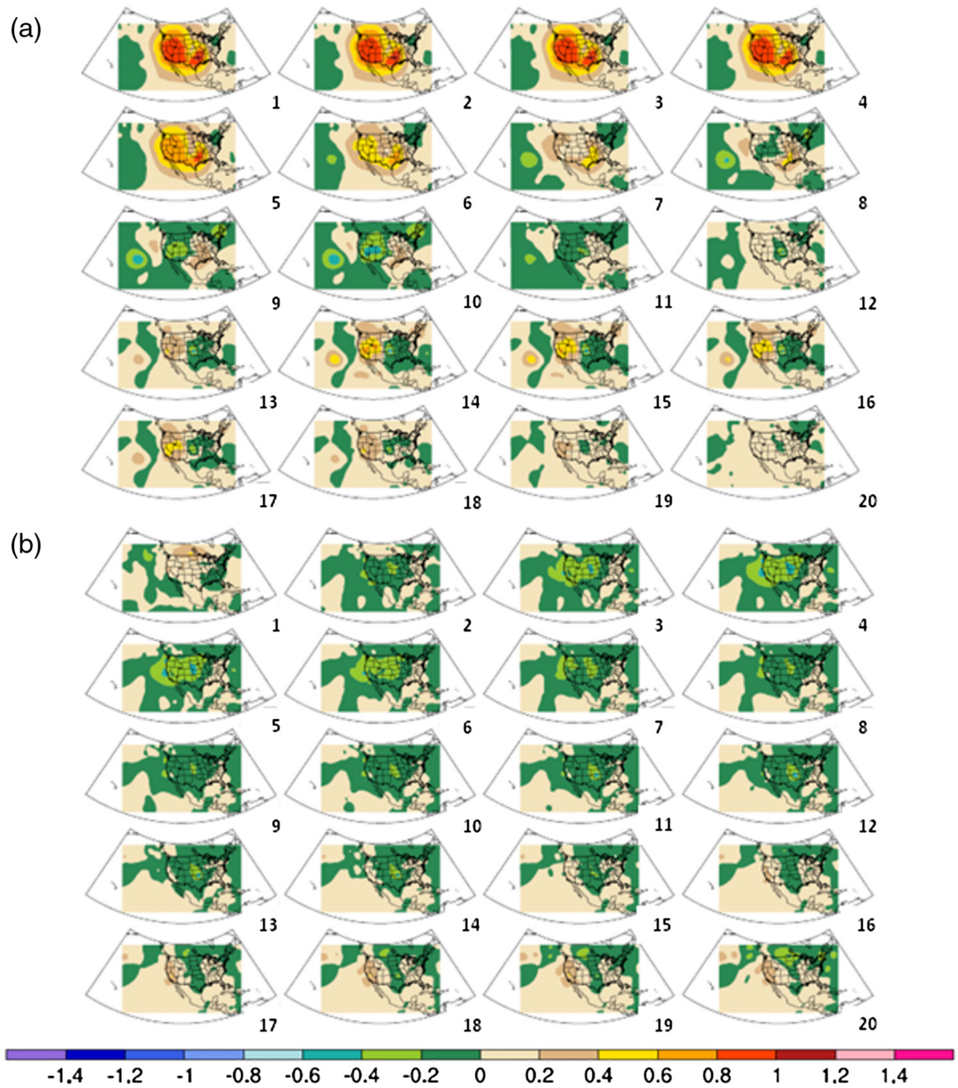

Fig. 5 Temperature analysis increments (K) for assimilating conventional data with (a) regional **B** matrix and (b) global **B** matrix. Stratosphere levels from 2 (subplot 1) to 100 hPa (subplot 20).

increments was selected. This was the set with the smallest temperature analysis increments in the stratosphere.

The analysis increments for a PSOT when the tuned **B** matrix was used are shown in Fig. 6. Compared with the PSOT using the provided **B** matrices, the tuned **B** matrix resulted in smaller analysis increments in the vicinity of the perturbation. The horizontal spatial influence of temperature, u-component, and v-component of wind were also reduced by about a third, accompanied by a decrease in increment magnitude. The vertical radius of influence was also reduced for the u-component of wind.

3.3 *Bias Correction*

Measured satellite radiances are compared with their equivalents computed from a short-term forecast or an analysis estimate of the atmospheric state using a radiative transfer model to monitor for biases. In doing so, it is assumed that the observed satellite radiances are free from calibration errors, the radiative transfer model is accurate, and the short-term forecast provided by NWP model is free from systematic error. However, these assumptions are not always valid. Biases vary with time (both diurnally and seasonally), geography or airmass, scan position of satellite instrument, and the position of the satellite around its orbit.[32] In variational data

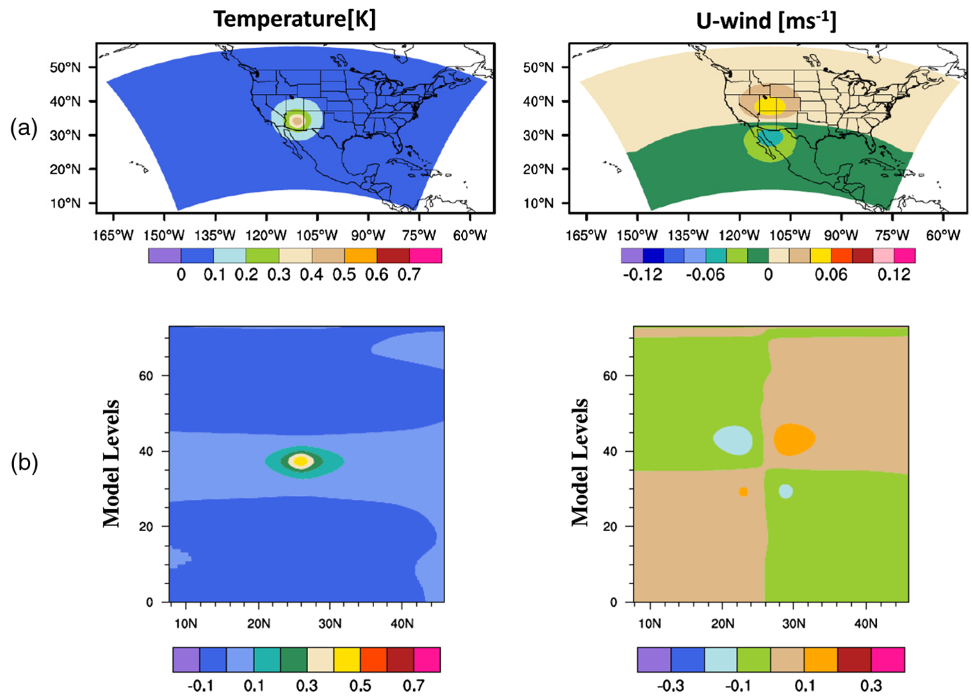

Fig. 6 Analysis increment on the (a) *xy* plane and (b) *yz* plane for a single temperature observation at 34°N, −111°E and 250 hPa (σ level 37) obtained from using a tuned **B** matrix. The difference between the temperature observation and the background state was 1 K. Observational error was set to 1 K.

assimilation, both the observation and background errors are assumed to be unbiased and normally distributed. Histograms of innovations before and after the bias correction are indicative of how well the bias correction worked. A nonzero mean of the O–F distribution indicates the presence of bias. The bias correction is not perfect. It is working properly if the mean of the innovation distribution after bias correction is very close to zero.

The bias correction is made up of two components: scan angle bias and airmass bias. In the GSI, a variant of the variational bias correction (VarBC) method described by Ref. 13 is used. In our version of GSI, only the air mass component was included in the variational scheme. Scan angle bias, which was slowly varying in time, is a 30-day running mean. The airmass component was modeled using five predictors. These predictors were offset (constant), path length, integrated lapse rate, square of integrated lapse rate, and cloud liquid water. The cloud liquid water predictor was only used in the microwave airmass bias correction. The airmass component was dynamically updated during each assimilation cycle. In this study, the scan angle bias came from the NCEP regional data assimilation system of June 8, 2012. The preference of a more recent set of bias coefficient files, as opposed to those valid for the experiment time period i.e., May 17, 2008, was to keep the CRTM version consistent with that in the version of GSI being used. The scan angle bias was not updated during these experiments. This was a reasonable assumption, as the scan angle bias was not expected to change much during these experiments. The airmass coefficients were initialized at each of the first assimilation cycles (T-12) with the airmass coefficients from the NCEP regional operational system of June 8, 2012. The airmass coefficient file was updated during subsequent assimilation cycles through T-0.

Figure 7 shows the departures of observations from the first guess with and without applying the bias correction for representative channels used in this study. Applying the bias correction (red curve) shifted the mean of the O–F distribution close to zero.

In our regional data assimilation experiments, we also found that the bias correction and QC of the radiance observations were interdependent as stated by Aulígné and McNally.[33] Screening of radiance observations was thus critical to ensure that analyses were not degraded. QC of the radiance observations to be assimilated was performed on bias-corrected innovations. If the bias correction technique improperly changed the bias of the observations, the QC procedures, such as the gross error check, might then exclude good data and accept the bad data into the assimilation system. If not controlled, the positive feedback between the bias correction and the QC could substantially degrade the NWP analysis. In regional data assimilation, success of the bias correction is highly sensitive to the bias coefficients.

4 Results

4.1 *Analysis Statistics*

As data QC procedures were applied to the bias-corrected radiance observations, the performance of the QC procedures can be evaluated by examining the innovation distribution. Taking IR radiances as an example, brightness temperatures of cloudy observations are much lower than when they are clear. Innovation in this case will be negative because the simulated brightness temperature from the first guess assumes clear sky conditions. Cloud detection procedures will need to be tightened if cold tails are present in the O–F distributions.

Figures 7(b), 7(d), and 7(f) show innovation histograms of surface channels. For surface channel observations, uncertainty in emissivity can lead to large O–F values. Assimilation of such observations could be reduced by restricting the range of the innovation values, also known as relative departure checks. Due to emissivity uncertainty, the number of surface channels that are assimilated is much lower compared with the nonsurface channels, especially

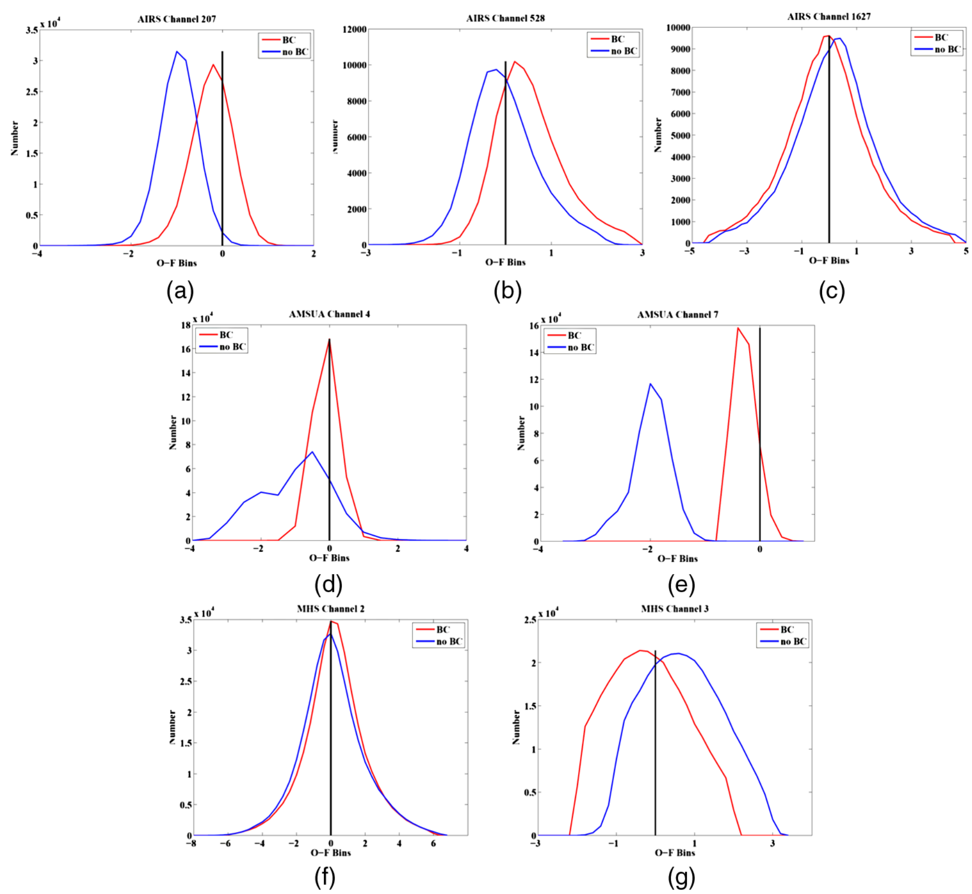

Fig. 7 Histograms of observation–first guess (O–F) before and after bias correction (BC) for (a) AIRS temperature channel that peaked at 410 hPa, (b) AIRS surface channel, (c) AIRS water vapor channel that peaked at 500 hPa, (d) NOAA-18 AMSU-A channel 4 (surface), (e) NOAA-18 AMSU-A channel 7 (tropospheric), (f) NOAA-18 MHS channel 2 (surface), and (g) NOAA-18 MHS channel 3 (moisture). Blue curve indicates before bias correction and red curve is after bias correction. The black line is the zero line.

over land. From Figs. 7(c) and 7(g), the bias correction technique had also worked for the water vapor channels.

An indication that radiance observations were properly fitted was when average of analysis error [observation (O) – analysis (A)] after bias correction was close to zero. The standard deviation (σ) of O–A after bias correction was an indication if observations were assimilated optimally. The O–A standard deviation should be larger than the NEDT of the channel to avoid overfitting of observations. This was to account for representativeness errors, radiative transfer model errors, instrument limitations, and interpolation errors. Radiance observations were overfitted if the NEDT was larger than the standard deviation of O–A.

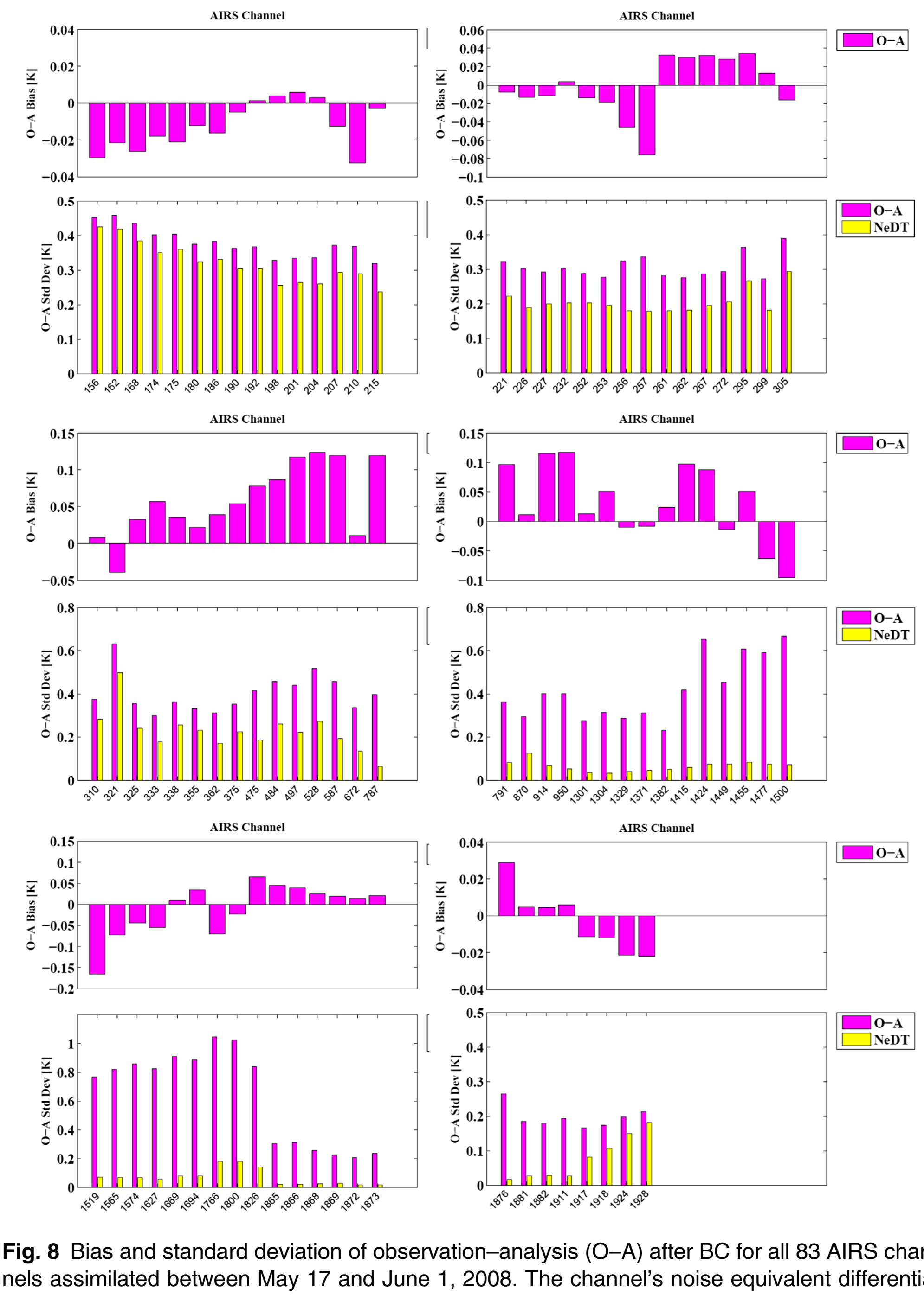

Fig. 8 Bias and standard deviation of observation–analysis (O–A) after BC for all 83 AIRS channels assimilated between May 17 and June 1, 2008. The channel's noise equivalent differential temperature in yellow was rescaled from the reference temperature of 250 K to the temperature of the atmospheric layer, where the channel had the largest sensitivity.

Bias and the standard deviation of analysis error for all 83 AIRS channels assimilated are shown in Fig. 8. The channel number in the abscissa was labeled according to the AIRS 2378 channel set. Channel numbers less than 475 were the 15 μm CO_2 temperature sounding channels, 475 to 1326 were surface and near surface channels, 1327 to 1864 were water vapor channels, and the remaining were 4.3-μm CO_2 channels. As seen from this figure, radiances from temperature sounding channels were well fitted, with O–A biases not exceeding 0.08 K. The biases were negative for most of the channels in the 15-μm CO_2 band, indicating the observations were generally cooler than the analysis. For channels in 4.3 μm, the biases were positive. Biases in surface and water vapor channels were larger. Standard deviation of channel O–A was all larger than the NEDT, implying that none of the AIRS channels were overfitted. The NEDT plotted had been rescaled from the reference temperature of 250 K to the temperature of the layer, where the channel had the greatest sensitivity. The standard deviation of temperature sounding channels ranged between 0.3 and 0.4 K; surface channels were on average about 0.4 K and water vapor channels were close to 1 K. The other radiances used in these experiments were also tested for overfitting (not shown). These plots show no change in bias or standard deviation compared to the other radiance observation with the addition of AIRS, suggesting that assimilating AIRS observations had not degraded the fit of other observations. An increase in bias was observed in the MHS channels. This could be caused by the bias observed in the AIRS water vapor channels.

Geographical distributions of bias and standard deviation of O–F and O–A after bias correction for AIRS channels indicated that the largest biases with respect to first guess were over land for both temperature (Fig. 9) and surface channels (Fig. 10). After assimilation, the biases were reduced, most significantly over the ocean. Smaller reductions in O–A over land were observed, as observations over land were assimilated with less weight due to uncertainty in emissivity, resulting in smaller incremental changes. The standard deviation varied similarly to the biases, with greater reductions in standard deviation over the ocean. For water vapor channels (Fig. 11), the bias was independent of the surface properties. Mean of O–A for water vapor channels was smaller than that of O–F. Pronounced improvement over the ocean was seen in the standard deviation after assimilation. Similar improvements were also noted for other sensors.

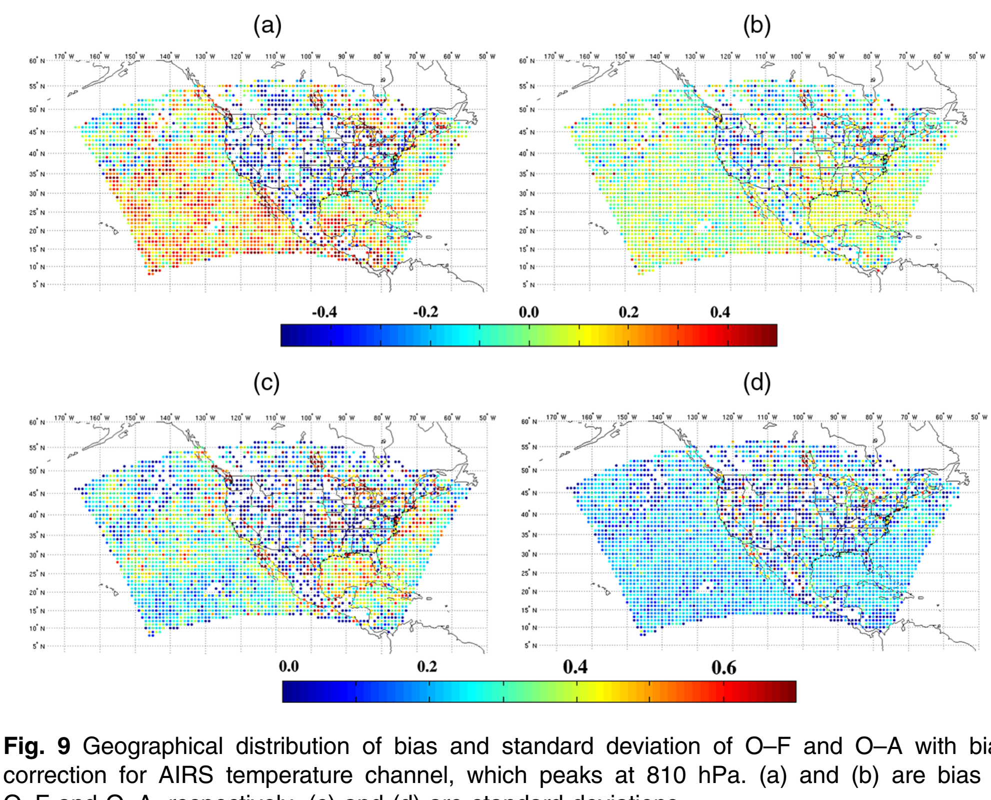

Fig. 9 Geographical distribution of bias and standard deviation of O–F and O–A with bias correction for AIRS temperature channel, which peaks at 810 hPa. (a) and (b) are bias of O–F and O–A, respectively. (c) and (d) are standard deviations.

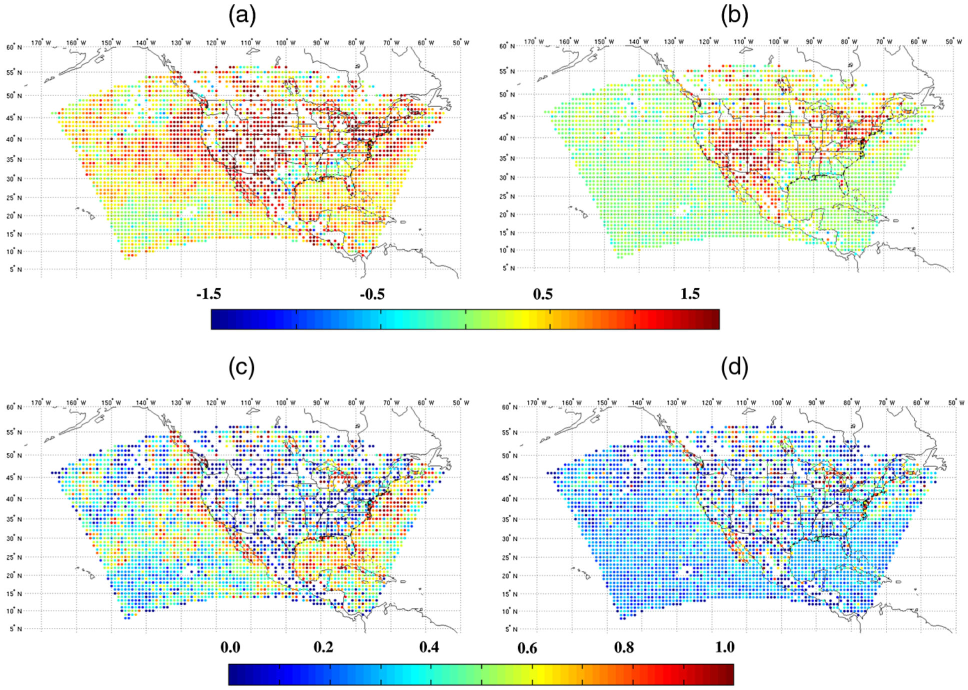

Fig. 10 Geographical distribution of bias and standard deviation of O–F and O–A with bias correction for AIRS surface channel. (a) and (b) are bias of O–F and O–A, respectively. (c) and (d) are standard deviations.

In data assimilation, observations typically make small corrections to short-term forecasts. The analyzed corrections (analysis increments) could reveal a lot about the performance of the assimilation system. The presence of large mean increments was an indication of bias, and it could be caused by the observations or the model.

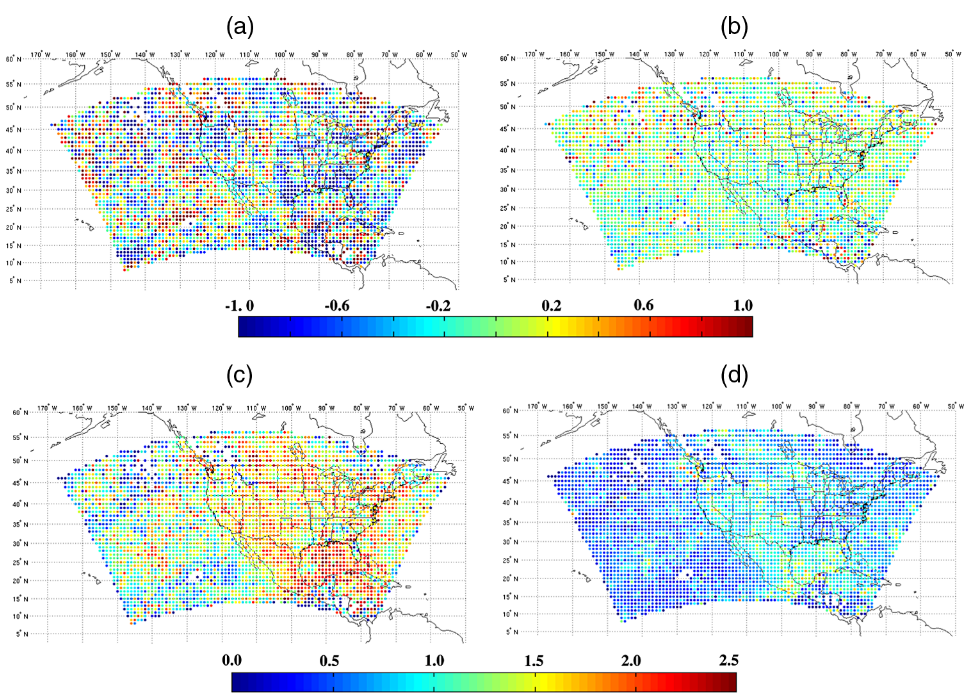

Fig. 11 Geographical distribution of bias and standard deviation of O–F and O–A with bias correction if AIRS water vapor channel which peaks at 500 hPa. (a) and (b) are bias of O–F and O–A, respectively. (c) and (d) are standard deviations.

Figure 12 shows the analysis increments of various atmospheric variables plotted at their representative levels. Moisture was important in the lower troposphere, thus 850 hPa was chosen. Temperature and geopotential height were shown in mid troposphere (500 hPa). U-component of wind, being the stronger wind component, was plotted at the jet level of 250 hPa. The analysis increments were average values from all assimilation experiments ending at 12 UTC, that is to say T-0 is at 12 UTC. Column (a) was the average analysis increments for the CNTRL and column (b) was for the EXP. Column (c) was the change in standard deviation with the addition of AIRS data. Negative values implied that the standard deviation was improved with the assimilation of AIRS radiances. Modifications of the RH field by the assimilation of AIRS data were concentrated in two regions, the Eastern Pacific and upper Midwest, where the mean moisture increments increased. Another large negative mean increment over the southeast region of Contiguous United States (CONUS) was also identified in both the CNTRL and EXP; thus, it was not caused by the addition of AIRS data. Geopotential height was related to temperature; therefore, improvement made to the temperature field with the addition of AIRS data over CONUS was also reflected in geopotential heights. An increase in mean analysis increments for temperature along the west coast was identified in the geopotential height field. As AIRS is an IR sensor, radiance measurements are related to temperature and humidity. Any changes in the wind field due to AIRS assimilation were brought about by the dynamical constraints in the **B** matrix. Significant increments were seen in the jet level in the CNTRL but minimal

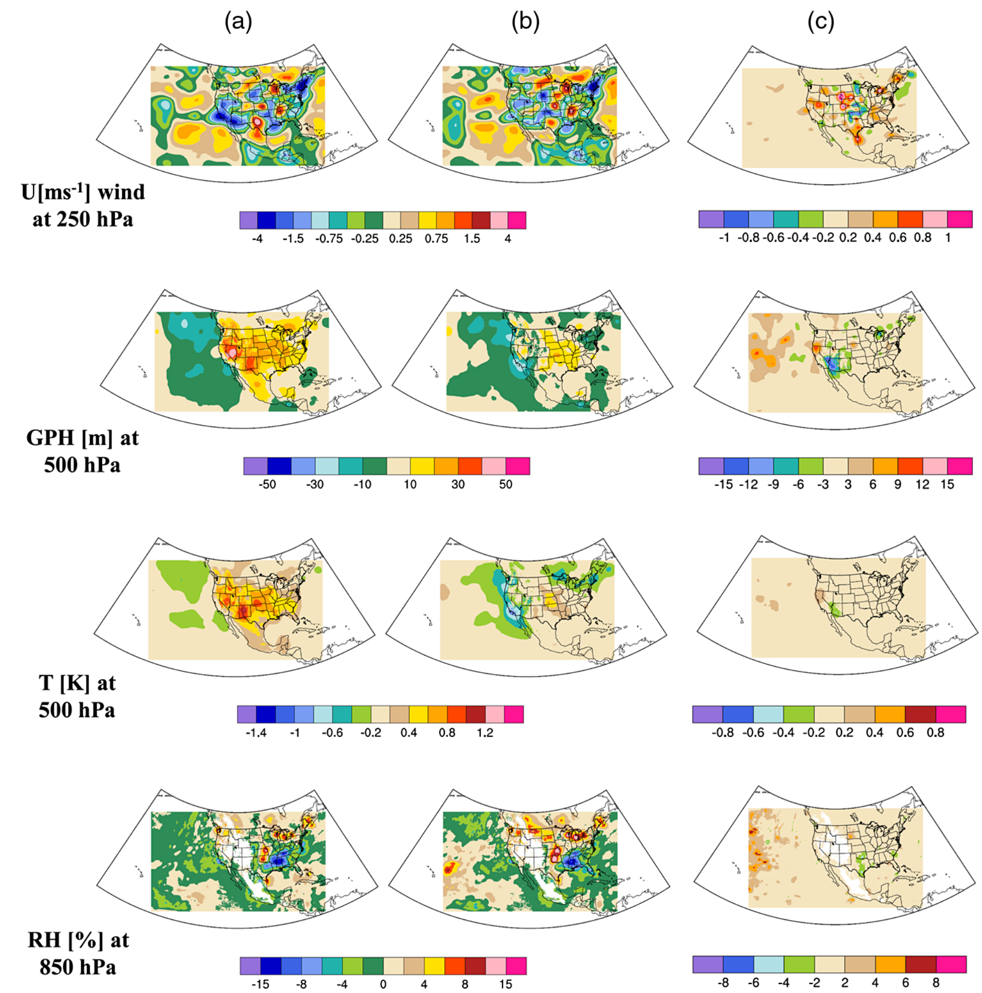

Fig. 12 Statistics of analysis increments for assimilation experiments ending at 12 UTC: (a) mean analysis increment without AIRS assimilation (CTRL), (b) mean analysis increment with AIRS assimilation (EXP), and (c) difference in standard deviation between with and without AIRS assimilation. Negative values indicate reduction in standard deviation and positive values imply increase in standard deviation.

reduction in mean analysis increments were noted after the addition of AIRS data. There were only five AIRS channels that peaked between 200 and 300 hPa. The small number of AIRS temperature channels at this level was insufficient to improve the bias. The poor definition of the tropopause also contributed to the lack of improvement. Changes in standard deviation were small except for geopotential height, where regions of increased standard deviation were correlated with regions of increased mean temperature increments.

The mean and standard deviation of analysis increments plotted in Fig. 13 were calculated from analyses whose assimilation experiments ended at 18 UTC. The mean temperature and geopotential height increments increased with the assimilation of AIRS data in these experiments. This was opposite to the experiments ending at 12 UTC. Similar trends were observed for moisture increments over the eastern part of the model domain. Standard deviations also increased over the regions, where large mean increemnts were evident. Large wind biases were observed at the jet level (250 hPa). Regions of larger mean analysis increments with the assimilation of AIRS data matched up with the AIRS overpass time over the domain. Regions where there was bias reduction in temperature analysis increments could be due to the propagation of information from observations from earlier cycles.

The analyses without AIRS assimilation were subtracted from the analyses with AIRS to obtain the impact due to AIRS. The corrections due to AIRS were over the regions of

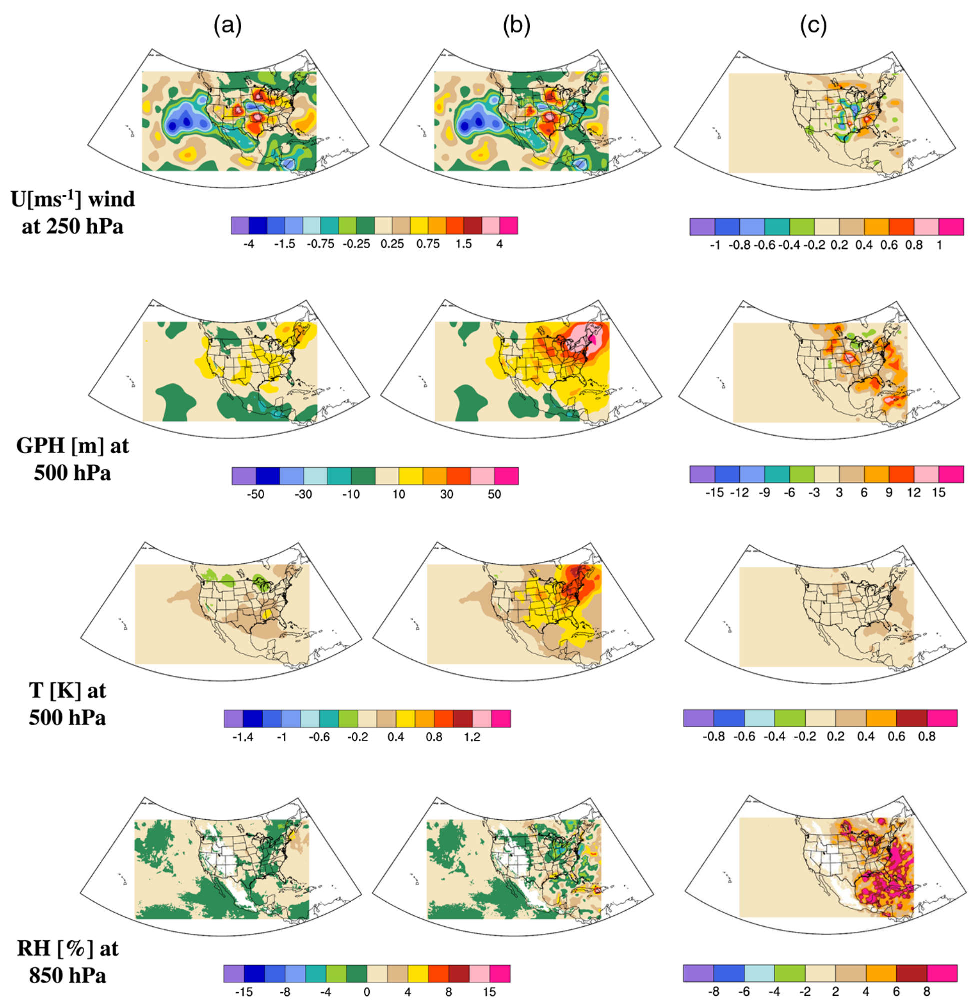

Fig. 13 Statistics of analysis increments for assimilation experiments ending at 18 UTC: (a) mean analysis increment without AIRS assimilation (CTRL), (b) mean analysis increment with AIRS assimilation (EXP), and (c) difference in standard deviation between with and without AIRS assimilation. Negative values indicate reduction in standard deviation and positive values imply increase in standard deviation.

AIRS overpasses. Statistics of analysis increments from experiments ending at 00 and 12 UTC were consistent with each other. Experiments ending at 06 and 18 UTC were also consistent with each other. For 00/12 UTC, assimilation of AIRS did not create any significant bias. In the 06/18 UTC analyses, the existence of a cold bias aloft and warm bias in the lower atmosphere created a less stable atmosphere (Fig. 14). This might lead to more clouds being generated in the forecast. This could be due to the larger biases in the AIRS water vapor channels or that the cloud detection over this region was deficient in identifying these cloudy radiances.

Alternatively, the larger difference in analysis increments might be due to the lack of rawinsondes at asynoptic times, which were weighted heavily in assimilation systems. This allowed AIRS to create a larger influence, as the latest observations had the most impact on the assimilation system.

4.2 *Forecast Statistics*

The observations used for verification included model analyses, rawinsondes, satellite radiance observations not assimilated, and accumulated precipitation measurements. Approximately 1200 rawinsonde profiles over CONUS were used for verification. Forecasts were verified through 36 h. From Fig. 15, there was a consistent improvement in temperature bias with the assimilation of AIRS radiances between 400 and 700 hPa all the way out to 36 h. The most significant improvements were at 500 and 700 hPa. At 850 hPa, temperature improvements were seen out to 24 h, but the temperature improvements at 200 hPa were only for ranges out to 12 h. Between 300 and 700 hPa, observed temperatures were cooler than the predicted temperatures. At 300 and 700 hPa, forecast errors at the 6, 18, and 30 forecast hours were larger than that at 12, 24, and 36. This was due to biases in the analyses. The standard deviation between

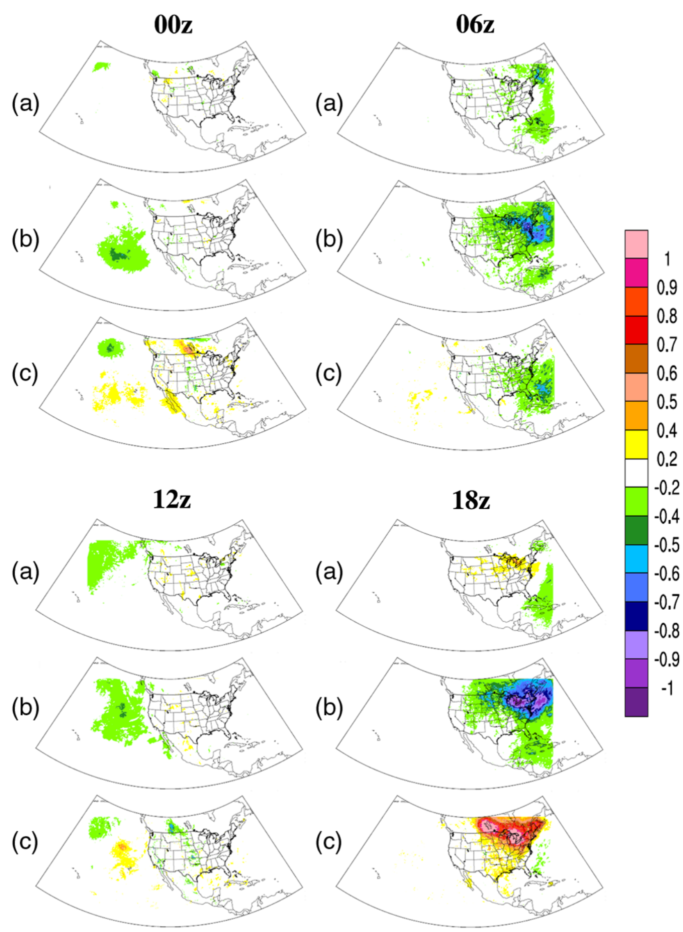

Fig. 14 Average of the difference between EXP analyses and CNTRL analysis for temperature at (a) 300 hPa, (b) 500 hPa, and (c) 850 hPa at different synoptic times.

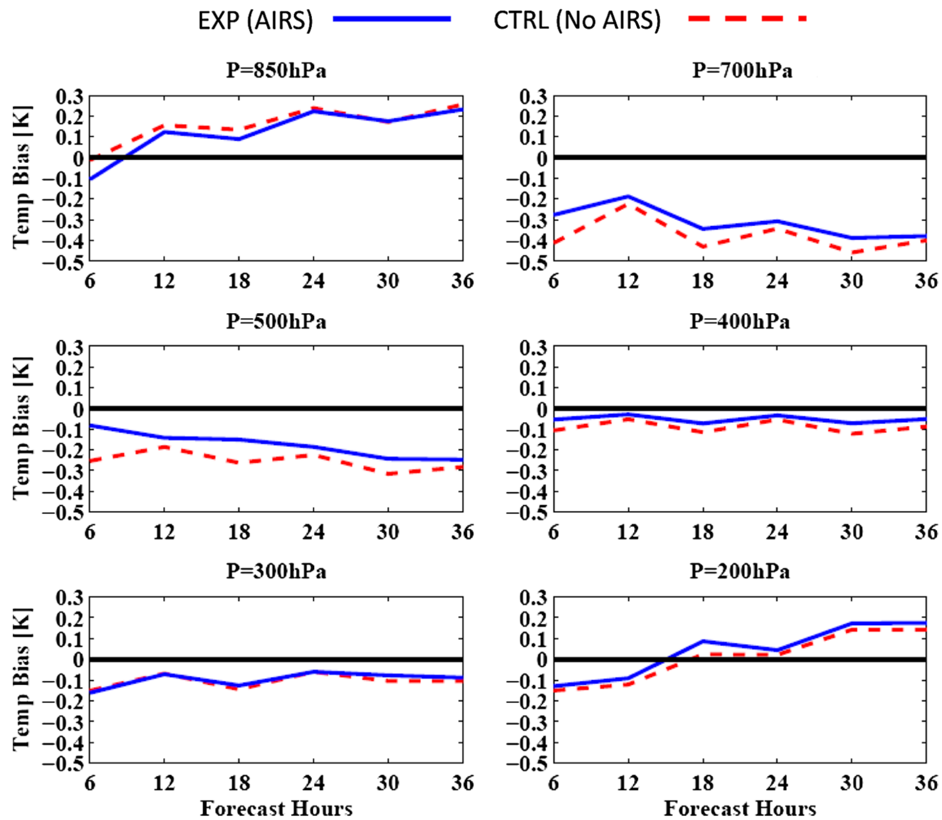

Fig. 15 Temperature bias for rawinsonde verification for CNTRL (no AIRS) and EXP (AIRS) at different forecast hours for different pressure levels.

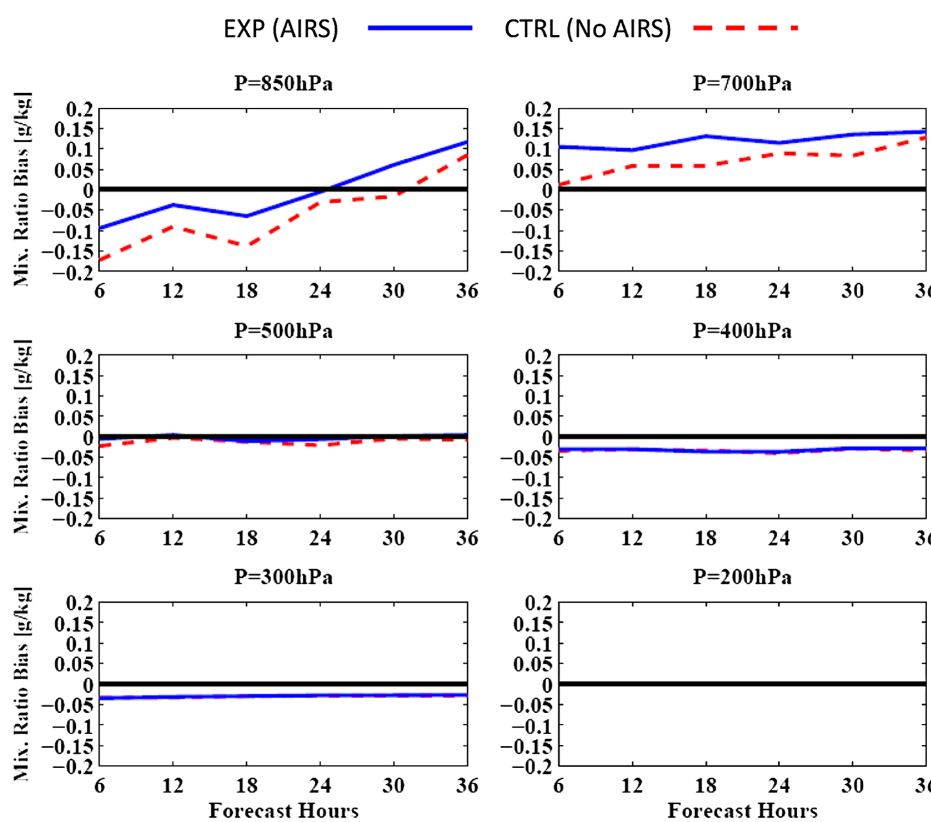

Fig. 16 Bias of mixing ratio for rawinsonde verification for CNTRL (no AIRS) and EXP (AIRS) at different forecast hours for different pressure levels.

rawinsondes and model profiles changed little and in most cases there was a slight increase in the spread with the assimilation of AIRS data. The standard deviations also increased with forecast hours, this was consistent with model errors growing over time.

For moisture (Fig. 16), there was an improvement in bias with the assimilation of AIRS at 850 hPa for the first 24 h. The opposite was true at 700 hPa. The increase in bias at 700 hPa could be attributed to the bias introduced by the assimilation of AIRS data in the mid troposphere. The standard deviation in moisture (not shown) was not affected by the AIRS assimilation. Model error growth was also apparent with increasing forecast time.

Forecast fields were also compared with observed satellite measurements through simulated brightness temperatures. These satellite observations were treated as independent observations, as they were not assimilated. A 30-min window was used to constrain the observation time. It was assumed that observed radiance within this window coincides with the forecast time. To reduce errors introduced due to land emissivity uncertainty, only observations over water surface were used in the verification. Plotted in Fig. 17 is the bias of O–F with no bias correction for different AMSU-A channels at different forecast hours. Slight improvement in forecast error was observed except for channels 3, 12, 13, and 15. Channels 3 and 15 are surface channels. Though emissivity uncertainty was reduced by using only ocean observations, for microwave, emissivity was modeled as a function of model wind speed by the CRTM. Errors in wind speed could affect the modeled emissivity and thus the simulated brightness temperature. Channels 12 and 13 are stratospheric channels. Presence of biases in the analyses in the upper atmosphere influenced the forecasts in this region. In addition, very few AIRS stratospheric channels were assimilated due to significant contribution above the model top. Standard deviation of forecast error was small with increasing spread over time. Forecast error was consistent over time, as radiances are vertically integrated quantities, thus less sensitive to the variation of temperature and moisture at individual pressure levels.

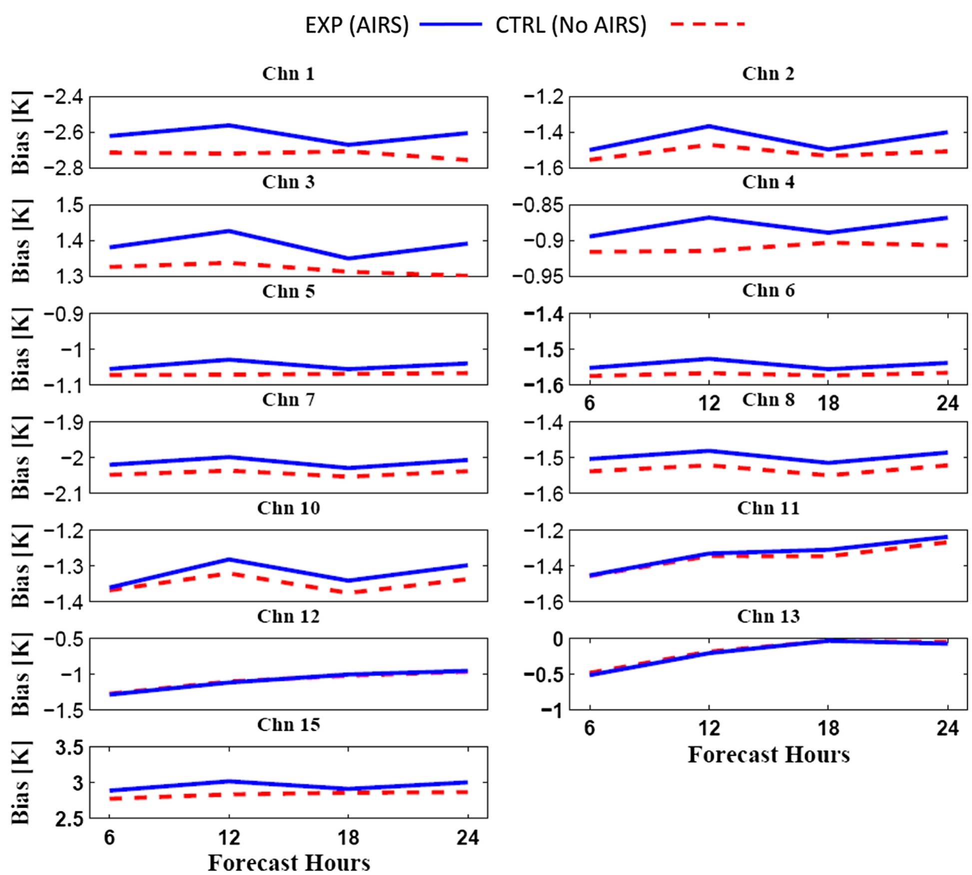

Fig. 17 Bias between observed and simulated brightness temperatures for all channels on NOAA-18 AMSU-A at different forecast hours.

Simulated brightness temperatures using the forecast fields were also verified with observations from AMSU-A on NOAA-15, and the results were consistent with that obtained from NOAA-18.

To evaluate which forecast was closer to the analysis, the forecast impact (FI)[34] was used. Equation (1) is the two-dimensional FI for a given pressure level:

$$\mathrm{FI}(x,y) = 100 \times \frac{\sqrt{\frac{\sum_{i=1}^{N}(C_i - A_i)^2}{N}} - \sqrt{\frac{\sum_{i=1}^{N}(D_i - A_i)^2}{N}}}{\sqrt{\frac{\sum_{i=1}^{N}(D_i - A_i)^2}{N}}}. \tag{1}$$

The variables C and D are the forecasts from CTRL and EXP, respectively. A is the 00-h analysis from CTRL, which is valid at the same forecast time. N is the number of diagnostic days. The first term in the numerator of Eq. (1) is the error of the control forecast. The second term in the numerator of Eq. (1) is the error in the AIRS forecast. The normalization factor is the error in the AIRS forecast. The improvement or degradation with respect to the root mean square error of the AIRS forecast is given in percentage. The geographical distribution of the FI were presented. Regions of positive and negative impact could then be evaluated. Positive FI implied that the forecast compared more favorably to its corresponding analysis with AIRS included than with it denied. FI for 500 hPa, temperature was plotted in Fig. 18 for 6, 12, 18, 24, 30, and 36-h forecasts. Positive impact was observed over the Eastern Pacific up to 30 h. The largest impact was at the 6-h forecast. Rate of decrease in impact was most rapid from 6 to 12 h.

Some positive FI was seen in RH at 850 hPa for the first 6 h, but approached neutral after that. For other atmospheric variables, positive impact up to 18 h was seen in some parts of the domain

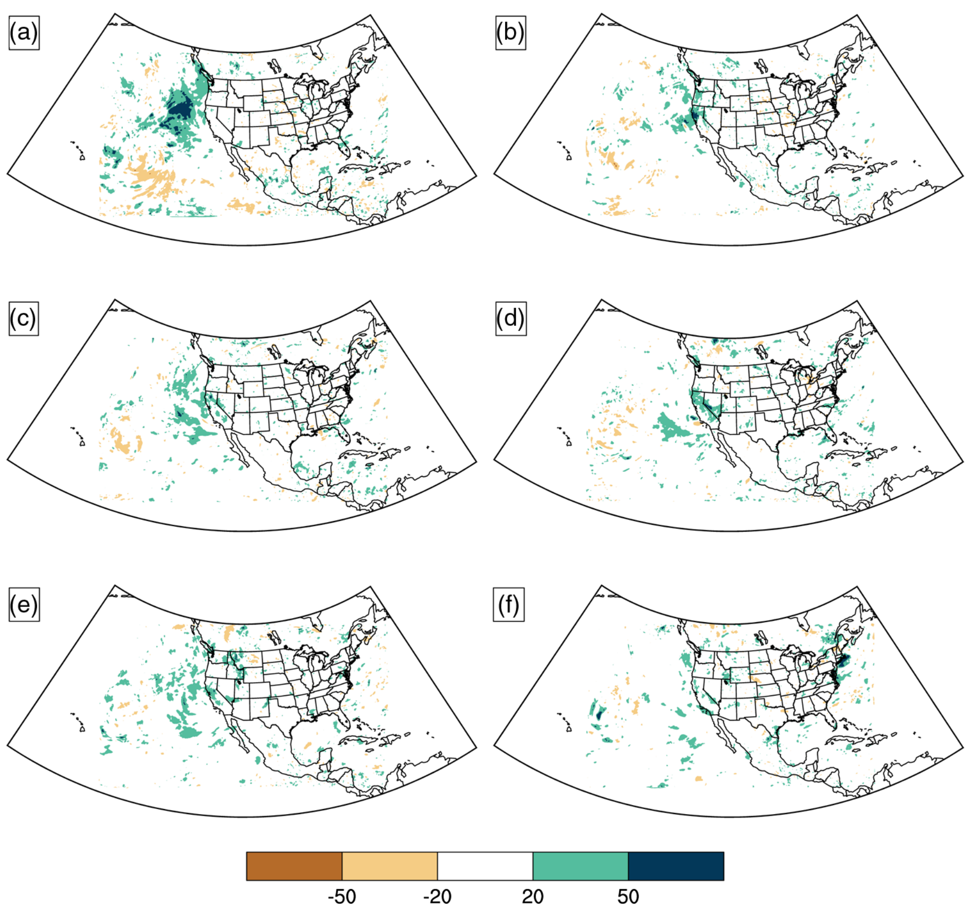

Fig. 18 Forecast impact in percentage for 500-hPa temperature at different forecast hours derived using forecasts initiated from 12 UTC analyses. (a) 6, (b) 12, (c) 18, (d) 24, (e) 30, and (f) 36.

for u-component of wind at 500 hPa. However, the negative impact with assimilation of AIRS was seen in precipitable water.

The 24-h–accumulated precipitation was verified against the NCEP National Stage IV Precipitation analysis. Precipitation analyses were provided by NCAR Earth Observing Laboratory under sponsorship of the National Science Foundation. Twenty-four hour–accumulated precipitation skill scores were evaluated. The model was given 6 h to spin up its precipitation, thus the 24-h–accumulated precipitation forecast spanned from the 6th forecast hour to the 30th forecast hour. The skill scores used to assess the performance of assimilating clear sky AIRS radiances on precipitation are frequency bias and the equitable threat score (ETS) as explained in Refs. 35 and 36. Plotted in Fig. 19 were both frequency bias and ETS for all four synoptic times, where the 36-h forecasts were initiated. A bias greater than 1 indicated the model is generating more precipitation than observed. The bias varied little with the assimilation of AIRS for 00 UTC and 06 UTC. At 12 UTC, the addition of AIRS increased the bias for very heavy precipitation. As for 18 UTC, the bias was larger with the assimilation of AIRS across all thresholds. This was consistent with the biases that were seen in the analysis increments and forecast increments for 18 UTC experiments. Very little impact was seen for ETS. Significant testing for each synoptic time was carried out using a Monte Carlo significance test.

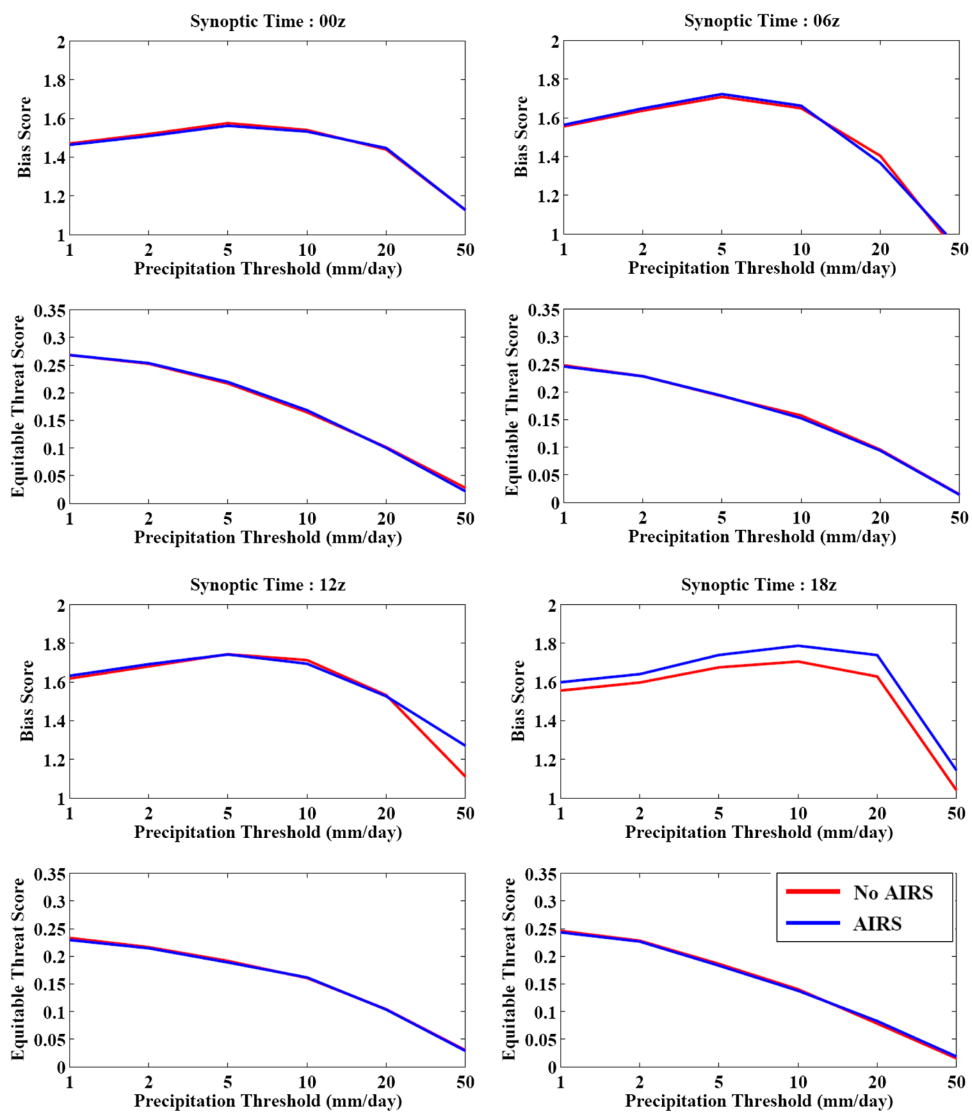

Fig. 19 Frequency bias and equitable threat score for 24-h accumulated precipitation for different precipitation thresholds. The different synoptic time indicates the start of the 36-h forecasts.

Ten thousand Monte-Carlo simulations of frequency bias and ETS were computed by randomly selecting samples of hits, false alarms, misses, and correct rejections from values used to compute frequency bias and ETS plotted in Fig. 19. Difference in frequency bias and ETS between CNTRL and EXP were statistically insignificant.

5 Summary

In this study, a limited-area NWP model with the community GSI and WRF was used. Both conventional and satellite data were assimilated in the control. Satellite data included in the control were radiances from AMSU-A, MHS, and HIRS-4. The experiment contained all the data used in the control plus the clear sky AIRS radiances. A total of 83 AIRS channels were assimilated in this study. A cold start was initiated at T-12 with the GFS global analysis at all four synoptic times. Five assimilation cycles were performed at 3-h intervals prior to running a 36-h forecast. The AIRS assimilation experiment was conducted over a period of 16 days.

As the community versions of GSI and WRF were not obtained from an operational center, they did not work together optimally without tuning. The design of an assimilation experiment required careful consideration of the various components of the assimilation process. Areas covered in this study include the forecast model domain configuration, the QC procedures for AIRS radiances, the background error covariance matrix, and the bias correction tuning. The considerations made in these areas are summarized as follows:

- Global models provide the initial conditions and LBCs needed by regional models. To slow down the propagation of errors from the boundaries caused by interpolating from a coarse-resolution model to high resolution, a large domain within limits imposed by available computer resources was selected for this study.
- Only clear AIRS radiances were assimilated in this study. They were identified via an AIRS cloudmask generated using MODIS cloud products and the various IR cloud checks within the GSI.
- The **B** matrix spreads information from observations, controls the percentage of innovation being added to the analysis, and maintains dynamically consistent increments between model variables. Tests of a pseudo single observation, assimilation of conventional data only, and assimilation of both conventional and satellite data were carried out to select and tune the precomputed **B** matrices prior to running assimilation experiments. The final tuned **B** matrix had smaller lengthscales and produced smaller analysis increments compared with the original **B** matrix.
- A VarBC technique was used to bias-correct satellite radiance observations. Histograms of bias-corrected innovations for temperature, surface, and water vapor sensitive channels had near zero mean and approximately Gaussian distribution, indicating that the bias-correction technique worked as expected. In addition, there were very few innovation outliers, implying that QC procedures used were sufficient in rejecting bad observations.

Bias and standard deviation of innovation and analysis error indicated that the largest improvement with assimilation of AIRS occurred over the ocean. Less improvement was seen over land due to land surface emissivity uncertainty. Statistics of analysis increments indicated that there were larger temperature increments concentrated in the northeast corner of the domain in the 06/18 UTC analyses compared with the 00/12 UTC analyses with the assimilation of AIRS radiances. This could be caused by unidentified cloudy observations. An alternative explanation for the larger difference in analysis increments at asynoptic times may be the lack of rawinsondes that have very high weights in the assimilation system, thus allowing the AIRS observations to have more influence. Though the assimilation runs over a 12-h period, the latest arriving observations had the most impact on the assimilation system.

Verification of forecasts against rawinsondes indicated consistent improvement in temperature bias between 400 and 700 hPa up to 36 h when EXP forecasts were compared with the CNTRL forecast. For moisture, assimilation of AIRS radiance observations had reduced the bias in mixing ratio at the lower troposphere (850 hPa) for a time period of 24 h.

However, an increase in moisture bias was evident at 700 hPa. This could be linked to the bias introduced by assimilating observations from AIRS water vapor channels in the mid troposphere. The standard deviation between forecasts and observations changed very little with and without the assimilation of AIRS radiances. Forecast fields were transformed to brightness temperatures and compared with observed satellite measurements for AMSU-A on NOAA-15 and NOAA-18. These satellite observations were treated as independent observations as they were not assimilated. Though results showed only small improvement in brightness temperature bias, this positive improvement was observed for most channels except surface and stratospheric channels. Degradation in surface channels was most likely due to surface emissivity uncertainty and stratospheric channels could be caused by poorer forecasts in this region of the atmosphere. FI was used as a measure to evaluate which forecast was closer to the analysis. Temperature, moisture, and u-component of wind field showed positive FI spanning from 6 to 30 h into the forecast. Precipitation skill scores varied little with the AIRS radiance assimilation. Overall, results from this study suggested that the assimilation of clear sky AIRS radiance observations in regional models had a small positive impact.

The limited use of AIRS stratospheric channels in this study and the minimum impact from the assimilation of water vapor channels are two areas to be explored in future. Investigations on increasing the model top of regional models by using the spectral analyses from the global model, instead of the postprocessed grib files, are underway to increase the use of AIRS stratospheric channels. Methods to better improve water vapor assimilations are also being looked into.

Acknowledgments

The authors wish to thank Wan-shu Wu and Mark Iredell of NOAA/NCEP for providing insight and advice on the tuning of the data assimilation and forecast system. The experiments were run on the NOAA/NESDIS Supercomputer for Satellite Simulations and data assimilation Studies (S4) located at the University of Wisconsin–Madison. This work was supported under NASA Grant NNX11AH63G. The authors also wish to thank the two anonymous reviewers whose comments helped to improve the manuscript.

References

1. H. H. Aumann and R. J. Pagano, "Atmospheric infrared sounder on the earth observing system," *Opt. Eng.* **33**(3), 776–784 (1994), http://dx.doi.org/10.1117/12.159325.
2. H. Aumann et al., "AIRS/AMSU/HSB on the Aqua mission: design, science objectives, data products, and processing systems," *IEEE Trans. Geosci. Remote Sensing* **41**(2), 253–264 (2003), http://dx.doi.org/10.1109/TGRS.2002.808356.
3. H.-L. Huang, W. L. Smith, and H. M. Woolf, "Vertical resolution and accuracy of atmospheric infrared sounding spectrometers," *J. Appl. Meteorol.* **31**(3), 265–274 (1992), http://dx.doi.org/10.1175/1520-0450(1992)031<0265:VRAAOA>2.0.CO;2.
4. H.-L. Huang and R. J. Purser, "Objective measures of the information density of satellite data," *Meteorol. Atmos. Phys.* **60**(1–3), 105–117 (1996), http://dx.doi.org/10.1007/BF01029788.
5. NRC, *Issues in the Integration of Research and Operational Satellite Systems for Climate Research*, Vol. 1, National Academy Press, Washington, DC (2000).
6. E. S. Maddy and C. D. Barnet, "Vertical resolution estimates in Version 5 of AIRS operational retrievals," *IEEE Trans. Geosci. Remote Sens.* **46**(8), 2375–2384 (2008), http://dx.doi.org/10.1109/TGRS.2008.917498.
7. A. P. McNally et al., "The assimilation of AIRS radiance data at ECMWF," *Q. J. R. Meteorol. Soc.* **132**(616), 935–957 (2006), http://dx.doi.org/10.1256/qj.04.171.
8. T. Auligné and F. Rabier, "Assimilation results for AIRS at Météo-France," in *ECMWF Workshop on Assimilation of High Spectral Resolution Sounders in NWP*, pp. 89–92, Shinfield Park, Reading (2004).
9. J. Cameron, A. Collard, and E. Stephen, "Operational use of AIRS observations at the Met Office," in *14th Int. TOVS Study Conf.*, pp. 731–737, China, Beijing (2005).

10. J. Le Marshall et al., "Improving global analysis and forecasting with AIRS," *Bull. Am. Meteorol. Soc.* **87**(7), 891–894 (2006), http://dx.doi.org/10.1175/BAMS-87-7-891.
11. B. Ruston et al., "Assimilation of AIRS data at NRL," in *15th Int. TOVS Study Conf.*, pp. 156–161, Maratea, Italy (2006).
12. L. Garand et al., "Implementation of AIRS assimilation at MSC," presented at *EUMETSAT Meteorological Satellite Conf.*, Amsterdam, The Netherlands (2007).
13. T. Auligné, A. P. McNally, and D. P. Dee, "Adaptive bias correction for satellite data in a numerical weather prediction system," *Q. J. R. Meteorol. Soc.* **133**, 631–642 (2007), http://dx.doi.org/10.1002/(ISSN)1477-870X.
14. W. McCarty, G. Jedlovec, and T. L. Miller, "Impact of the assimilation of atmospheric infrared sounder radiance measurements on short-term weather forecasts," *J. Geophys. Res.* **114**(D18), D18122 (2009), http://dx.doi.org/10.1029/2008JD011626.
15. F. Hilton et al., "Assimilation of IASI at the Met Office and assessment of its impact through observing system experiments," *Q. J. R. Meteorol. Soc.* **135**, 495–505 (2009), http://dx.doi.org/10.1002/qj.v135:639.
16. W. C. Skamarock et al., "A description of the advanced research WRF version 3," Technical Report, National Center for Atmospheric Research (2008), http://www.mmm.ucar.edu/wrf/users/docs/arw_v3.pdf.
17. T. T. Warner, R. A. Peterson, and R. E. Treadon, "A tutorial on lateral boundary conditions as a basic and potentially serious limitation to regional numerical weather prediction," *Bull. Am. Meteor. Soc.* **78**(11), 2599–2617 (1997), http://dx.doi.org/10.1175/1520-0477(1997)078<2599:ATOLBC>2.0.CO;2.
18. W.-S. Wu, R. J. Purser, and D. F. Parrish, "Three-dimensional variational analysis with spatially inhomogeneous covariances," *Mon. Weather Rev.* **130**(12), 2905–2916 (2002), http://dx.doi.org/10.1175/1520-0493(2002)130<2905:TDVAWS>2.0.CO;2.
19. D. T. Kleist et al., "Introduction of the GSI into the NCEP global data assimilation system," *Weather Forecasting* **24**(6), 1691–1705 (2009), http://dx.doi.org/10.1175/2009WAF2222201.1.
20. "Gridpoint Statistical Interpolation (GSI) Version 3.0 User's Guide," Developmental Testbed Center, Community GSI System (2011), http://www.dtcenter.org/com-GSI/users/docs/index.php (21 March 2014).
21. D. T. Kleist et al., "Improving incremental balance in the GSI 3DVAR analysis system," *Mon. Weather Rev.* **137**(3), 1046–1060 (2009), http://dx.doi.org/10.1175/2008MWR2623.1.
22. Y. Han et al., "JCSDA community radiative transfer model (CRTM) version 1," Technical Report 122, NOAA, Washington DC (2006).
23. F. Z. Weng, "Advances in radiative transfer modeling in support of satellite data assimilation," *J. Atmos. Sci.* **64**(11), 3799–3807 (2007), http://dx.doi.org/10.1175/2007JAS2112.1.
24. Y. Chen et al., "On water vapor Jacobian in fast radiative transfer model," *J. Geophys. Res.* **115**, D12303 (2010), http://dx.doi.org/10.1029/2009JD013379.
25. Y. Chen, Y. Han, and F. Weng, "Comparison of two transmittance algorithms in the community radiative transfer model: application to AVHRR," *J. Geophys. Res.* **117**, D06206 (2012), http://dx/doi.org/10.1029/2011JD016656.
26. J. Susskind, C. D. Barnet, and J. M. Blaisdell, "Retrieval of atmospheric and surface parameters from AIRS/AMSU/HSB data in the presence of clouds," *IEEE Trans. Geosci. Remote Sens.* **41**(2), 390–409 (2003), http://dx.doi.org/10.1109/TGRS.2002.808236.
27. R. E. Holz and S. A. Ackerman, "Arctic winter high spectral resolution cloud height retrievals," in *Proc. 14th AMS Conf. Satell. Meteorol. Oceanogr.*, Atlanta, Georgia (2006).
28. J. Li et al., "Optimal cloud-clearing for AIRS radiances using MODIS," *IEEE Trans. Geosci. Remote Sensing* **43**(6), 1266–1278 (2005), http://dx.doi.org/10.1109/TGRS.2005.847795.
29. S. A. Ackerman et al., "Discriminating clear sky from clouds with MODIS," *J. Geophys. Res.* **103**(D24), 32141–32157 (1998), http://dx.doi.org/10.1029/1998JD200032.
30. F. Bouttier and P. Courtier, "Data assimilation concepts and methods," Meteorological Training Course Lecture Series, ECMWF, Reading, United Kingdom (1999).
31. D. F. Parrish and J. C. Derber, "The national meteorological center's spectral statistical-interpolation analysis system," *Mon. Weather Rev.* **120**(8), 1747–1763 (1992), http://dx.doi.org/10.1175/1520-0493(1992)120<1747:TNMCSS>2.0.CO;2.

32. T. McNally, "Bias estimation and correction for satellite data assimilation," in *ECMWF/ EUMETSAT NWP-SAF Workshop Bias Estim. Data Assimilation*, pp. 21–39, ECMWF, Reading, United Kingdom (2006).
33. T. Auligné and A. P. McNally, "Interaction between bias correction and quality control," *Q. J. R. Meteorol. Soc.* **133**, 643–653 (2007), http://dx.doi.org/10.1002/(ISSN)1477-870X.
34. T. H. Zapotocny et al., "A four-season impact study of rawinsonde, GOES, and POES data in the Eta data assimilation system. Part I: The total contribution," *Weather Forecasting* **20**(2), 161–177 (2005), http://dx.doi.org/10.1175/WAF837.1.
35. I. T. Jolliffe and D. B. Stephenson, *Forecast Verification: A Practitioner's Guide in Atmospheric Science*, John Wiley & Sons Ltd., Chichester (2003).
36. WWRP, "Recommendations for the verification and intercomparison of QPFs and PQPFs from operational NWP Models- Revision 2 October 2008," Technical Report WMO/TD-No.1485, WMO (2008).

Agnes H. N. Lim received her PhD from the University of Wisconsin–Madison in 2013, and she is currently an assistant researcher at the Cooperative Institute for Meteorological Satellite Studies, Space Science and Engineering Center at the University of Wisconsin–Madison. Her current research work focuses on regional data assimilation of hyperspectral infrared satellite data for current and future sensors.

James A. Jung received his PhD from the University of Maryland in 2008 specializing in data assimilation. He is a scientist with the Cooperative Institute for Meteorological Studies and an adjunct professor at the University of Wisconsin–Madison.

Hung-Lung Allen Huang received his PhD in the area of satellite remote sensing from the University of Wisconsin–Madison in 1989. In the same year, he joined Cooperative Institute for Meteorological Satellite Studies, Space Science and Engineering Center, University of Wisconsin–Madison, and currently a distinguished scientist of the UWMadison, a Fellow of International Society for Optical Engineering (SPIE), and an adjunct professor of several universities.

Steve A. Ackerman is an associate dean of physical sciences and a professor in the Department of Atmospheric and Oceanic Sciences at the University of Wisconsin–Madison. He is the director of the Cooperative Institute for Meteorological Satellite Studies (CIMSS), a collaboration between UW-Madison and NOAA/NESDIS. His research experience includes remote sensing, radiative transfer, Earth radiation budget, cloud radiative parameterizations, climate change, and aerosol studies.

Jason A. Otkin is an assistant scientist at the Cooperative Institute for Meteorological Satellite Studies and the Space Science and Engineering Center at the University of Wisconsin–Madison specializing in remote sensing applications for high-resolution numerical modeling, data assimilation, model validation, and drought monitoring.